

1 **Changes in seismic attenuation due to fracturing and fluid migration during the**  
2 **2016-2017 Central Italy seismic sequence**

3

4

5 <sup>1,2\*</sup>Simona Gabrielli, <sup>1</sup>Aybige Akinci, <sup>1</sup>Guido Ventura, <sup>3</sup>Ferdinando Napolitano, <sup>4,5</sup>Edoardo  
6 Del Pezzo and <sup>2,6</sup>Luca De Siena

7

8 1) Istituto Nazionale di Geofisica e Vulcanologia, Via di Vigna Murata 605, 00143  
9 Roma, Italy

10 2) University of Aberdeen, School of Geosciences, Meston Building, Aberdeen, AB24  
11 3UE, Scotland, UK

12 3) Università degli Studi di Salerno, Dipartimento di Fisica "E.R. Caianiello", Via  
13 Giovanni Paolo II 132, 84084, Fisciano, SA, Italy

14 4) Istituto Nazionale di Geofisica e Vulcanologia, Osservatorio Vesuviano, Via  
15 Diocleziano, 328, 80125, Napoli, Italy

16 5) Instituto Andaluz de Geofisica, Universidad de Granada, Calle del Prof. Clavera, 12,  
17 18071 Granada, Spain

18 6) Institute of Geosciences, Johannes Gutenberg University, J.-J.-Becher-Weg 21  
19 D-55128, University of Mainz, Germany

20

21 Corresponding author: Simona Gabrielli ([simona.gabrielli@ingv.it](mailto:simona.gabrielli@ingv.it))

22

23

24 **Key points:**

25 • 4D imaging of seismic scattering and absorption, before and during the 2016-2017 Amatrice-  
26 Visso-Norcia (Central Italy) seismic sequence

27 • Scattering imaging is highly influenced by lithological and structural features of the Central  
28 Apennines

29 • High-absorption anomaly is spatially related to deep CO<sub>2</sub>-bearing fluids, migrated along the  
30 fault network during each seismic sequence

31

32

33

34

35 **Abstract**

36 The Amatrice-Visso-Norcia seismic sequence struck Central Italy across the Apenninic normal faults  
37 system in 2016. Fluids likely triggered the sequence and reduced the stability of the fault network  
38 following the first earthquake (Amatrice,  $M_w6.0$ ), with their migration nucleating the Visso ( $M_w5.9$ )  
39 and Norcia ( $M_w6.5$ ) mainshocks. However, both spatial extent and mechanisms of fluid migration  
40 and diffusion through the network remain unclear. High fluid content, enhanced permeability and  
41 pervasive microcracking increase seismic attenuation, but each process contributes to different  
42 attenuation mechanisms. Here, we measured and mapped peak delay time and late-time coda  
43 attenuation, using them as proxies of seismic scattering and absorption before and during the  
44 sequence. Structural discontinuities and lithology control scattering losses at all frequencies, with the  
45 highest scattering delineating carbonate formations within the Gran Sasso massif. The Monti Sibillini  
46 thrust marks the strongest contrasts in scattering, indicating a barrier for northward fracture  
47 propagation. Before the sequence, low-frequency high-absorption anomalies distribute around the  
48 chain axis. A single high-absorption anomaly bounded north by the Monti Sibillini thrust develops  
49 NNW-SSE across the seismogenic zone during the sequence. This spatial expansion appears related  
50 to the deep migration of  $CO_2$ -bearing fluids across the strike of the fault network from a deep source  
51 of trapped  $CO_2$  near the Amatrice earthquake. Migration develops primarily during the Visso  
52 sequence, followed by diffusion across the fault zones during the Norcia sequence. High-scattering  
53 and high-absorption focus below the carbonates south of Norcia during the sequence, mapping the  
54 progressive northern permeation of the seismogenic zone from south to north.

55

56 **Plain Language Summary**

57 Central Italy is characterized by significant seismic sequences, as the one of the 2016-2017 across the  
58 Apennine Chain, known as the Amatrice-Visso-Norcia sequence. Fluids migrating in the fault system  
59 have been already recognized as the trigger of this seismicity. However, the migration between the

60 faults of this mountain belt is not clear yet. Seismic attenuation (a description of how the seismic  
61 wave is losing energy during its path) can help in understanding the interaction between fluids and  
62 the fractures (e.g., faults). Here, we are looking at two seismic sequences, one between 2013 and 2016  
63 (pre) and one during the 2016-2017 sequence. We applied two different techniques, the peak delay  
64 time and the coda attenuation, that describe the amount of fractures and the presence of fluids in the  
65 medium, respectively. In our results, the former is controlled by the presence of faults and fractures  
66 in the lithologies, as the high scattering around the Gran Sasso massif, which is highly fractured. The  
67 coda attenuation imaging is showing, at different time periods, how the deep-CO<sub>2</sub> fluids migrated in  
68 each seismic sequence, focusing along the Central Apennine chain at the end of the Norcia  
69 mainshock.

## 70 **1. Introduction**

71 Between August and October 2016, 25,600 earthquakes ( $0.1 < M < 6.5$ ) struck the Central Apennines  
72 chain in Central Italy (Chiaraluca et al., 2017). Eight events had  $M_w > 5.0$ , with three mainshocks  
73 occurring near Amatrice ( $M_w$  6.0, August 24, 2016), Visso ( $M_w$  5.9, October 26, 2016) and Norcia  
74 ( $M_w$  6.5, October 30, 2016). The Amatrice-Visso-Norcia sequence (AVN) developed on the NNW-  
75 SSE-trending normal fault systems of Mt. Vettore (north) and Mt. Gorzano (south), activating a 70  
76 km x 10 km area trending parallel to the major axis of the central Apennines (Improta et al., 2019).  
77 The fault mechanisms were consistent with the extension of the central Apennines, which coexists  
78 with the opening of the Tyrrhenian back-arc basin (Chiaraluca et al., 2017). Digital seismic networks  
79 were deployed immediately after the Amatrice earthquake, recording events with  $M > 0.1$ , and making  
80 the AVN the best-monitored earthquake sequence striking Italy. The AVN has been modelled as a  
81 cascading rupture triggered by fluids entering the fault systems (Walters et al., 2018). Multiple  
82 mainshock sequences are common features in the Apennines (Improta et al., 2019 and reference  
83 therein). This phenomenon is a consequence of the complex interactions between adjacent faults and  
84 triggering processes that include static and dynamic stress transfer between faults, pores fluid pressure

85 migration and co-seismic release of a deep source of trapped CO<sub>2</sub> (Chiarabba et al., 2009a; Malagnini  
86 et al., 2012; Miller et al., 2004).

87 Seismic waves lose their energy when travelling through complex fluid-filled fault networks  
88 (Sketsiou et al., 2021). Seismic attenuation tomography has thus the potential to image the effect of  
89 increased fluid content and migration. Chiarabba et al. (2009a) used P- and S-wave attenuation to  
90 track fluid migrations across the Central-Northern Apennines fault networks, identifying them as the  
91 driving mechanism of the cause of the 1997 Umbria-Marche seismic sequence. Sketsiou et al. (2021)  
92 imaged total attenuation across the Pollino range (Southern Italy), identifying two fluid reservoirs  
93 hosting fluids that laterally migrated at depth, producing the 2010-2014 Pollino seismic sequence  
94 (Brozzetti et al. 2017, and references therein). Waves attenuate due to scattering and absorption (Sato  
95 et al., 2012). The increase of seismic absorption relative to scattering losses and of their frequency  
96 dependence supports the inference of fluids permeating faults during the AVN (Akinici et al., 2020).

97 Scattering and absorption can be mapped in space using two seismic attributes:

98 (1) the peak delay time, defined as the time difference between the S-wave arrival and the maximum  
99 amplitude of the event (Takahashi et al., 2007)

100 (2) the attenuation of coda waves ( $Q_c^{-1}$ ). Coda waves are wave-trains coming after the S wave-  
101 packet, and  $Q_c$  quantifies the decay rate of the coda envelope with increasing lapse time from the  
102 origin time of the earthquake (Aki and Chouet, 1975).

103 At crustal-scale and in the far field, peak delay measures multiple forward scattering due to random  
104 inhomogeneities (Takahashi et al., 2007; Calvet et al., 2013). The Markov approximation (Saito et  
105 al., 2002) can model its variations in space and frequencies at frequencies higher than 1 Hz. Takahashi  
106 et al. (2007) first used peak delay times to map volcanic areas in northeast Japan. High peak delays  
107 mark fractured volumes across the Pyrenees (Calvet et al., 2013), the eastern portion of the Siletz  
108 terrane in the Western US (De Siena et al., 2016), and the Vrancea region in Romania (Borleanu et  
109 al., 2017). Within fault networks, peak delay increases are visible at all frequencies when waves cross

110 fractured geological volumes, as the carbonates of the Pollino seismic gap, in Southern Italy  
111 (Napolitano et al., 2020).

112 Single scattering, multiple scattering and diffusion can model coda wave envelopes depending on  
113 frequency, lapse time and scale of the heterogeneities encountered during propagation (Sato et al.,  
114 2012). At late lapse times, coda waves can enter the diffusive regime, where coda attenuation is  
115 theoretically equal to absorption ( $Q_c = Q_i$  - Shapiro et al., 2000). Calvet and Margerin (2013)  
116 demonstrate that this assumption is valid for an onset time of the coda of 80s and epicentral distances  
117 between 0 and 90 km across the Pyrenees.  $Q_c^{-1}$  strongly depends on frequency in active tectonic  
118 regions (Sato et al., 2012). At low frequencies, high  $Q_c^{-1}$  anomalies map surface geology and  
119 sedimentary basins in the Pyrenees (Calvet et al., 2013), the Alps (Mayor et al., 2016) and Vrancea  
120 (Borleanu et al., 2017). At higher frequencies, the change in coda composition from surface to body  
121 waves can increase depth sensitivity (Mayor et al., 2016; De Siena et al., 2016; Gabrielli et al., 2020).  
122 This effect appears predominant when measuring  $Q_c^{-1}$  across volcanic structures, as at Mount St.  
123 Helens volcano (US). Here, low-frequency waves map the shallowest, most-heterogeneous volcanic  
124 structures, while deep feeding systems appear as high- $Q_c^{-1}$  anomalies at higher frequencies (De Siena  
125 et al., 2016; Gabrielli et al., 2020).

126 High peak delays and high  $Q_c^{-1}$  detect intrusions in mountain chains (Calvet et al., 2013) and  
127 magmatic systems (De Siena et al., 2016). These parameters are reliable marker of fluid-induced  
128 fracturing leading to earthquakes at the regional scale (Borleanu et al., 2017). In fault networks like  
129 those ruptured by the AVN, Napolitano et al. (2020) found that high-scattering and high-absorption  
130 patterns obtained by increasing frequencies map the migration of the historical seismic events from  
131 the 16<sup>th</sup> century up to the Pollino seismic sequence. This work supported the view that lateral fluid  
132 migrations cause the sequence (Brozzetti et al., 2017, and references therein). However, the temporal  
133 potential of joint scattering and absorption mapping in fault networks is still unexplored.

134 In this study, we measure and map peak delays and  $Q_c^{-1}$  in the 2D space. Due to the consistent spatial  
135 extent of the earthquakes, we repeat the mapping in time using data recorded:

- 136 1) between 2013 and 2016 (hereafter, pre-sequence), before the first mainshock of August 24, 2016,  
137  $M_w$ 6.0 Amatrice earthquake;
- 138 2) between August 2016 and January 2017 (hereafter, sequence) using data from the entire AVN;
- 139 3) during three different periods starting from the three main shocks: Amatrice (August 24, 2016 -  
140 October 26, 2016), Visso (October 26, 2016 - October 30, 2016) and Norcia (October 30, 2016 -  
141 January 18, 2017).

142 We offer insight into fluid migration and expansion processes leading and controlling a seismic  
143 sequence using peak delay and coda attenuation as frequency-dependent proxies of scattering loss  
144 and absorption.

## 145 **2. Geological and seismological background**

146 The Central Apennines is governed by the opening of the back-arc Tyrrhenian basin (west), the  
147 eastern migration of the compressive front, and the lithospheric plate's flexural retreat dipping below  
148 the Italian peninsula (Di Luccio et al., 2010). The Western Tyrrhenian is marked by thin crust (25  
149 km), high heat ( $> 200 \text{ mWm}^{-2}$ ), and positive gravity anomalies. Most of the Quaternary volcanoes  
150 and the geothermal areas (such as Larderello, Amiata, Campi Flegrei and Vesuvius) are activated by  
151 the perturbation of the mantle wedge (Ventura et al., 2007). On the contrary, the eastern part of the  
152 Adriatic Sea is marked by low heat flow and negative gravity anomalies. The average crustal  
153 thickness is thicker, around 35 km (Carminati and Doglioni, 2012).

154 The Central Apennine region is mainly composed of thrust sheets imbricated toward the Adriatic Sea,  
155 having a NW-SE trend, and creating a contact between the Meso-Cenozoic carbonate succession and  
156 the Miocenic flysch (Billi and Tiberti, 2009, and references therein). The sequence of carbonate rocks  
157 and terrigenous units can be traced from the surface to a depth of 8-10 km moving from east to west  
158 (Billi and Tiberti, 2009, and references therein). The Monti Sibillini thrust (also known as Olevano-  
159 Antrodoco thrust) in the southern sector of the Umbrian Arc has a NNE-SSW trend and it is causing  
160 the Sabina Miocene pelagic sediments to overthrust the Lazio - Abruzzi carbonate platform (Billi and

161 Tiberti, 2009). The Laga Formation (consisting of Messinian siliciclastic foredeep deposits) overlies  
162 both the Triassic - Miocene Lazio - Abruzzi platform and the Umbria - Marche pelagic succession  
163 (**Figure 1**) (Di Bucci et al., 2021, and references therein). Further east, the contact between the Laga  
164 Formation and the carbonate platform coincides with the E-W thrust of the Gran Sasso chain, bounded  
165 by the Monti Sibillini thrust to the west and the Morrone thrust to the east (Billi and Tiberti, 2009).  
166 Large intermountain basins as those of Amatrice, Norcia and Castelluccio are filled by Plio-  
167 Quaternary continental sediments (**Figure 1**). They formed due to Plio-Quaternary NW-SE striking  
168 normal faulting, which dissects the Apennine chain and partly reactivates the pre-existing older  
169 thrusts (Improta et al., 2019 and references therein).

170 Seismicity in the Apennines concentrates along the chain axis and manifests itself through swarms  
171 and sequences with events of magnitudes up to 7 and depths shallower than 10-15 km. The  
172 mainshocks have dip-slip, normal focal mechanisms consistent with ruptures along NW-SE striking  
173 fault planes moving in response to a NE-SW extension (Montone and Mariucci, 2016). Although  
174 some mainshocks nucleate in the crystalline basement underlying the chain at about 10 km depth,  
175 there are records of earthquakes in the overlying carbonates and sedimentary sequences. Seismic  
176 activity in the Central Apennines is modulated by deep-derived CO<sub>2</sub>-rich fluids, with gas releases  
177 triggering earthquakes (Miller et al., 2004; Di Luccio et al., 2010; Malagnini et al., 2012; Chiodini et  
178 al., 2004, 2020). Chiodini et al. (2020) show a record of 10 years (2009-2018) of tectonic CO<sub>2</sub>  
179 emissions compared with seismic activity in the Central Apennines (Italy), where devastating  
180 historical earthquakes (such as the 1461 event of L'Aquila, the 1703 event of Norcia - Montereale -  
181 L'Aquila and the 1915 M<sub>w</sub> 7.0 of Avezzano) occurred. Chiaraluce et al. (2007) and Collettini et al.  
182 (2008) reported overpressurized fluids in the deep wells of San Donato and Santo Stefano in the  
183 Apennines. Miller et al. (2004) propose that the 1997 Colfiorito aftershocks were caused by a co-  
184 seismic release of trapped high-pressure CO<sub>2</sub>. Chiarabba et al. (2009b) observed high velocity ratios  
185 during the foreshocks and aftershocks of the L'Aquila 2009 sequence (M<sub>w</sub>6.1), which allowed them  
186 to mark zones of high pore pressure and fluid enrichment. Malagnini et al. (2012) and Di Luccio et

187 al. (2010) showed that the diffusion of pore fluid pressure during the L'Aquila earthquake was caused  
188 by the activation of different fault segments visible through the spatial migration of seismic activity.  
189 In the Apennines, earthquakes with  $M > 5.5-6$  often rupture the surface so that fluids circulating in the  
190 shallower crust can enter and interact with the fault zone (Amoruso et al., 2011; Doglioni et al., 2014).  
191 The Central Apennines host large aquifers in the carbonate formations, such as the Gran Sasso  
192 (Amoruso et al., 2011) and the Nuria-Velino-Giano (Devoti et al., 2018) aquifers. The Gran Sasso  
193 aquifer registered short and mid-term changes in groundwater hydrodynamics (Amoruso et al., 2011)  
194 after the 2009 L'Aquila seismic event. The Gran Sasso aquifer has an extension of 700 km<sup>2</sup>, bounded  
195 by the Laga Formation to the north and east and by the low-permeable alluvial deposits to the west  
196 and south. The perennial groundwater reserves in this aquifer are estimated in the order of 10<sup>10</sup> m<sup>3</sup>,  
197 with a mean thickness of 1 km (Amoruso et al., 2011 and references therein). The 2016 Amatrice-  
198 Norcia seismic sequence generated an uplift of the water level both near the Gran Sasso (~1.8 m;  
199 Devoti et al., 2018) and as far as 100 km away from the mainshock area (up to 80 cm; Barberio et al.,  
200 2017). The Mounts Nuria-Velino-Giano hydrological complex is located ~40 km southwest of the  
201 Gran Sasso aquifer and has an outcropping area of about 1000 Km<sup>2</sup> (Chiodini et al., 2011 and  
202 references therein). It is bordered by low-permeability deposits and by the Mt. Sibillini thrust  
203 (Chiodini et al., 2011). Chiodini et al. (2011) performed a hydrogeochemical study of the Gran Sasso  
204 and Nuria-Velino-Giano aquifers to investigate the presence of a deep CO<sub>2</sub> source in the epicentral  
205 area of the 2009 L'Aquila seismic sequence. Both aquifers showed an increasing influx of fluids rich  
206 in deep CO<sub>2</sub> before and during the seismic sequence. Thus, deep high-pressure gas traps played a role  
207 in the generation of the L'Aquila seismic sequence, as previously modelled for the Colfiorito seismic  
208 event (Miller et al., 2004). Tomography images suggest that such traps occur at the base of the  
209 Apennine seismogenic layer, i.e., at the boundary between the upper and lower crust (at 10-15 km  
210 depth - Chiarabba et al., 2020).

211 AVN is ~30 km north of the L'Aquila area and ~50 km south of the hypocenter of 1997, M<sub>w</sub>6.0  
212 Umbria-Marche seismic sequence. The seismicity in this sector of the chain is associated to the Mt.

213 Vettore normal fault segments and the Mt. Gorzano fault (Monti della Laga fault system) (Buttinelli  
214 et al., 2018; Carminati et al., 2020; Brozzetti et al., 2019). The AVN ruptures the seismic gap between  
215 the 1997-98 Colfiorito (Chiaraluca et al., 2004) and the 2009 L'Aquila seismic sequences (Chiaraluca  
216 et al., 2011).

### 217 **3. Data and Methods**

#### 218 *3.1 Seismic dataset*

219 In the present study, we merged weak and strong-motion data from the AVN using earthquakes with  
220 magnitudes between 2.8 and 6.5. We selected earthquakes having a maximum depth of 20 km,  
221 keeping source-station distance within 100 km. The pre-sequence dataset comprises ~6000  
222 waveforms recorded at 47 seismic stations (**Figure 2a**). The complete data set for the AVN contains  
223 ~22000 waveforms recorded at 156 seismic stations (**Figure 2b**).

224 Strong ground motion data were registered by the accelerometric stations of the Italian strong motion  
225 network (RAN). Broadband weak-motion seismological stations are part of the Digital Seismic  
226 Network run by the Istituto Nazionale di Geofisica e Vulcanologia. The weak- and strong-motion  
227 accelerograms were downloaded from the Italian ACcelerometric Archive (ITACA) website, the  
228 European Strong Motion (ESM) database and the European Integrated Data Archive (EIDA)  
229 repository. The strong ground motion network is equipped with a three-component Kinometrics  
230 EpiSensor (FBA-3200 Hz) with a full-scale range of 1 or 2 g, combined with an ETNA 18 bits or K2-  
231 Makalu 24 bits digitizers. The weak-motion seismograms are corrected for instrument response. All  
232 the stations that registered only one seismic event were removed. The waveforms with P-wave travel  
233 times higher than 35 s were discarded from the database to constrain propagation within the crust.  
234 Waveforms with spikes, telemetry gaps and wave arrivals in the coda of the horizontal components  
235 of ground motion were manually removed. The dataset comprises seismograms with signal to noise  
236 ratio of the selected coda window higher than two. The P- and S-wave arrivals were picked manually

237 on each seismogram of the final dataset. The final dataset comprises ~4100 waveforms for the pre-  
238 sequence and ~13900 for the AVN.

239 The final AVN dataset has been further divided into three time periods, each following a mainshock  
240 recorded in 2016:

241 1) Amatrice sequence, comprising ~3600 waveforms recorded between August 24 and October  
242 26, 2016

243 2) Visso sequence, comprising ~1630 waveforms recorded between October 26 and October 30,  
244 2016

245 3) Norcia sequence, comprising ~8700 waveforms recorded between October 30 and January  
246 18, 2017.

247 Our study covers an area of 200 km x 220 km (lon: 11.85° - 14.25°; lat: 41.7° - 43.7°) and it is divided  
248 into 30x30 regularly spaced nodes. The seismograms were filtered with a band-pass Butterworth filter  
249 (4<sup>th</sup> order) in four frequency bands (1 – 2 Hz, 2 – 4 Hz, 4 – 8 Hz, and 8 – 16 Hz) centered at a  
250 frequency ( $f_c$ ) equal to 1.5, 3, 6 and 12 Hz. A Hilbert transform has been applied to compute the  
251 envelopes, which were then smoothed with a moving window of duration eight times the central  
252 frequency's inverse.

253 The open-access code Murat2D previously applied in volcanic (De Siena et al., 2016, 2017; Gabrielli  
254 et al. 2020) and tectonic settings (Borleanu et al., 2017; Napolitano et al., 2020) is used to perform  
255 all the analyses. The code is applied to datasets spanning five time frames: the pre-sequence (2013 –  
256 2016), the AVN and the three subsequences after the mainshocks (from August 24, 2016, to January  
257 18, 2017). Peak delay and  $Q_c^{-1}$  maps are interpreted separately and jointly in their parameter space  
258 (De Siena et al., 2016).

### 259 ***3.2 Peak delay measurements and mapping***

260 Seismic waves broaden in heterogeneous media due to multiple forward scattering. The delay  
261 between the S-wave onset and the maximum of the envelope increases with source-receiver distance

262 (Takahashi et al., 2007; Calvet and Margerin, 2013). The dependence of the peak delay time ( $t^{PD}(r)$ ,  
 263 in seconds) from hypocentral distance ( $R_{Hypo}$ , in km) is expressed by:

$$264 \quad \log_{10} t^{PD}(f) = A(f) + B(f) \cdot \log_{10} R_{Hypo} \quad (1)$$

265 where  $A(f)$  and  $B(f)$  in Eq. (1) are the coefficients of the resulting linear fit.

266 We selected seismograms with an  $R_{Hypo}$  between 20 and 100 km. For waveforms with  $R_{Hypo} < 20$  km,  
 267 the envelope broadening caused by the source duration prevails over scattering effects (Takahashi et  
 268 al., 2007). Measured peak delay times (black circles) and their dependence on hypocentral distance  
 269 are presented for the frequency band 1.5 Hz in **Figure S1**. The difference between the measured peak  
 270 delay time of the  $i$ -th waveform ( $t_i^{PD}(f)$ ) and the theoretical peak delay at the corresponding  
 271 hypocentral distance (Eq. 1) gives the amount of scattering accumulated along the raypath:

$$272 \quad \Delta \log_{10} t(f) = \log_{10} t_i^{PD}(f) - \log_{10} t^{PD}(f) \quad (2)$$

273 Positive values of  $\Delta \log_{10} t(f)$  represent high-scattering zones and heterogeneous portions of the  
 274 crust. In contrast, negative values mark low-scattering zones interpreted as rigid and compact crustal  
 275 areas (Takahashi et al., 2007). We mapped S-wave peak delays assuming source-receiver sensitivity  
 276 on rays and using a standard regionalization approach (Takahashi et al., 2007). **Figure S2** shows the  
 277 ray coverage for both pre-sequence and AVN datasets. The ray coverage is dense in the central sector  
 278 of the map; however, peak delay values spike in regions of low ray coverage. To avoid these trade-  
 279 offs in areas surrounding the seismogenic zone, we removed from the maps all nodes crossed by less  
 280 than ten rays (**Figure S3** - Calvet et al., 2013). The final maps are frequency-dependent, but we  
 281 assume no dependence on depth, as the earthquake dataset is entirely within the crust. At different  
 282 frequencies (wavelengths), we map heterogeneities of different dimensions.

### 283 **3.3 Coda attenuation measurements and mapping**

284 Aki and Chouet (1975) show that the power spectral energy density ( $E(t,f)$ ) is a function of the lapse  
 285 time from the earthquake's origin time ( $t$ ):

$$286 \quad E(t, f) = S(f) t^{-\alpha} \exp\left(\frac{-2\pi f t}{Q_c}\right), \quad (3)$$

287 where  $S(f)$  includes both source and site terms and  $Q_c^{-1}$  is the frequency-dependent inverse coda  
 288 quality factor.  $\alpha$  is equal to 3/2 if propagation is constrained within a single layer characterized by an  
 289 anisotropic multiple scattering regime (Paasschens, 1997; Calvet et al., 2013).  $Q_c^{-1}$  is computed by  
 290 linearizing Eq. (3). The linearization is computationally faster than non-linear grid-search algorithms  
 291 (e.g., Napolitano et al., 2020). The two approaches provide equivalent results when the signal-to-  
 292 noise ratio is higher than three and for coda windows longer than 10 seconds (Sketsiou et al., 2020,  
 293 and references therein).

294 Taking the logarithm of Eq. (3) and rearranging the terms, we can measure  $Q_c^{-1}$  using a straight-line  
 295 fitting:

$$296 \quad \frac{\ln[E(t,f) \cdot t^\alpha]}{2\pi f} = \frac{\ln[S(f)]}{2\pi f} - \frac{1}{Q_c} t \quad (4)$$

297 The  $Q_c^{-1}$  analysis window starts at twice the arrival time of the S wave and lasts 20 seconds. **Figure**  
 298 **S4** shows source-station measurements (black dots) and fitted (red line)  $Q_c^{-1}$  obtained using the AVN  
 299 dataset at 1.5 Hz. To image seismic absorption in the 2D space, we applied an inversion scheme (De  
 300 Siena et al., 2017) based on sensitivity kernel functions valid in the multiple-scattering regime (Del  
 301 Pezzo et al. 2018 – see **Figure S5**). We discuss the uncertainties relative to the onset of diffusion, the  
 302 theoretical background, and assumptions behind the use of coda sensitivity kernels, the inversion  
 303 strategy and resolution tests in the Supplementary Material Text and **Figures S6-S9**.

#### 304 **4. Results**

305 For both the peak delay and  $Q_c^{-1}$  spatial variation, the results are shown between 12.5° E – 13.7° E  
 306 and 42.15° N – 43.48° N, a zoom of the central part of the area in **Figure 2a, b**. Areas of high  
 307 resolution for peak delays and  $Q_c^{-1}$  are defined using hit counts (**Figure S3**) and the results of the  
 308 checkerboard tests (**Figures S7-S9**), respectively. We present the separate spatial variations of peak  
 309 delay and  $Q_c^{-1}$  using two different sets of maps (**Figures 3,4**). The final interpretation is performed  
 310 after separating measurements in their parameter space (**Figures 5** – De Siena et al., 2016)

#### 311 *4.1 Spatial variations of peak delays*

312 **Figures 3** show the spatial variation of the peak delay parameter (from here, scattering losses) as  
313 defined in Eq. (2) obtained at 1.5 Hz for the pre-sequence, the AVN and the three sub-sequences. The  
314 maps show the absolute value of the frequency-dependent peak delay,  $t^{PD}(f)$ : low and high scattering  
315 are the values below and above the 1.0 s, which is the average peak delay of the area. The results at  
316 higher frequencies are shown in **Figures S10-12**. High and low scattering losses correspond to hot  
317 (red) and cold (blue) colors, respectively. The pre-sequence and sequence maps (**Figures 3a,b**) show  
318 low scattering in the contact zone between the Meso-Cenozoic carbonate succession and the Miocenic  
319 flysch (Di Luccio et al., 2010). At higher frequencies (**Figures S11-12**), a high-scattering anomaly  
320 appears west of the mountain range. The primary scattering contrast defines the Gran Sasso formation  
321 in the pre-sequence, with low scattering northeast of the massif (Laga Formation domain) and high-  
322 scattering values southwest of it (L'Aquila basin) (**Figures 3a,b**).

323 We observe variations in scattering attenuation over different periods. During the pre-sequence, a  
324 low-scattering anomaly marks the northernmost area of the modelled fault planes. The area is  
325 characterized by high-scattering values during the Amatrice and Visso sequences and returns low  
326 scattering during the Norcia sequence. This area is delimited to the south by a thrust parallel to the  
327 Monti Sibillini thrust (**Figure 1**). Before the Amatrice earthquake, the area intersected by the AVN  
328 was marked by low scattering values (**Figure 3b**). During the Amatrice sequence, the southeastern  
329 part of the epicentral area becomes a low scattering region, while scattering increases northwest. In  
330 general, scattering losses increase and expand toward the epicentral area during the AVN. They  
331 progressively reach the southwestern patch of the Amatrice fault rupture area, spreading across the  
332 dense fault network west of Norcia during the Visso and Norcia sequences (**Figures 3a,b**).

333

#### 334 *4.2 Average and spatially varying $Q_c^{-1}$*

335 We report the frequency-dependent average  $Q_c^{-1}$  and their relative standard deviation for the pre-  
336 sequence and the AVN datasets in **Table 1**. These values are obtained from the best fit line of Eq.

337 (4).  $Q_c^{-1}$  decreases with frequency, as expected in tectonically active regions (de Lorenzo et al., 2013;  
 338 Akinici et al., 2020). Assuming a frequency-dependence given by  $Q_c^{-1} = Q_0^{-1} \cdot f^{-\eta}$ ,  $Q_c^{-1} =$   
 339  $(0.0075 \pm 0.0007) f^{(-0.74 \pm 0.10)}$  for the pre-sequence and  $Q_c^{-1} = (0.0076 \pm 0.0005) f^{(-0.76 \pm 0.07)}$  for the AVN.  
 340 While these values are comparable with those reported across the Apennines (de Lorenzo et al., 2013;  
 341 Sketsiou et al., 2021), the frequency-dependent  $\eta$  parameters correspond to the upper limit of the  
 342 range found by de Lorenzo et al. (2013) for the Central Apennines (0.65-0.75). In the assumption that  
 343  $Q_c^{-1} = Q_i^{-1}$  at late lapse time (Calvet and Margerin, 2013), we compare the results of **Table 1** with the  
 344  $Q_i$  calculated with the MLTWA by Akinici et al. (2020), who estimate  $Q_i(f) = (110 \pm 13) f^{0.9 \pm 0.2}$ . Both  
 345  $Q_0$  and  $\eta$  are within the uncertainties obtained with our method:  $Q_c(f) = (131 \pm 10) f^{(0.76 \pm 0.07)}$ .  
 346 **Figure 4a,b** present the spatial distribution of the  $Q_c^{-1}$  at 1.5 Hz obtained over the five periods. The  
 347 average  $Q_c^{-1}$  decreases with increasing frequency using all datasets, showing more intense spatial  
 348 variations at lower frequencies. The maximum  $Q_c^{-1}$  values are 0.015 at 1.5 Hz (**Figures 4a,b**) and  
 349 0.0027 at 12 Hz (**Figure S15**). At lower frequencies (1.5 - 3 Hz), there is a clear difference in the  
 350 anomaly patterns between the pre-sequence and the 2016-2017 dataset (**Figures 4a and S13a**) and  
 351 the individual seismic sequences (**Figures 4b**). High-absorption anomalies are widespread before the  
 352 Amatrice mainshock and focus on the fault zones during the AVN. The L'Aquila-Gran Sasso sector  
 353 shows a drastic decrease in attenuation during the AVN. The diffuse high absorption across the fault  
 354 network during the pre-sequence shifts further north after the Amatrice mainshock. High absorption  
 355 focuses on the dense fault network south of Norcia and the fault planes after the Visso mainshock  
 356 (rectangles in **Figure 4a,b**). After the Norcia mainshock, the NNW-SSE-trending high-absorption  
 357 anomaly expands across the Central Apennines range, bounded north and south by the Monti Sibillini  
 358 and Gran Sasso thrusts, respectively (**Figure 1**). The dense fault network south of Norcia shows a  
 359 substantial decrease of absorption at the end of the AVN compared to the Amatrice and Visso periods.  
 360 We identify a similar trend at high frequencies (**Figures S13-15**), with a more focused high anomaly  
 361 during each seismic sequence.

362 **4.3 Parameter separation maps**

363 Scattering and absorption measurements are combined by separating the spatially dependent  
364 measurements in color-coded ensembles (**Figure S16**). To do so, we removed the average values of  
365 peak delay and  $Q_c^{-1}$  at different frequency band from each single measurement of the datasets in each  
366 grid cell (De Siena et al., 2016; Napolitano et al., 2020). We plotted on a graph the relative variation  
367 of  $Q_c^{-1}$  on the horizontal axis and of  $\Delta\log_{10}(t)$  on the vertical axis (**Figure S16**) and presented in four  
368 quadrants with different colors. In this way, we provided a visual presentation of combined absorption  
369 ( $Q_c^{-1}$ ) and scattering (peak delay) attenuation patterns, characterizing each block in the map with the  
370 corresponding color.

371 Each color is an interpretation of the structures and their content in fluids as follows:

- 372 **1.** HS-HA (red): high scattering and high absorption define a fractured medium saturated in fluids;
- 373 **2.** LS-HA (orange): low scattering and high absorption describe a compact medium filled in fluids;
- 374 **3.** HS-LA (light blue): high scattering and low absorption characterize a dry and fractured medium;
- 375 **4.** LS-LA (green): low scattering and low absorption represent a dry and compact zone medium;
- 376 **5.** white marks areas with a level of discrimination less than 1% of the maximum variations.

377 The parameter maps at 1.5 Hz (**Figures 5a, b**) show two HS-HA anomalies NW and SE of the AVN  
378 epicentral areas in all periods. These anomalies coincide with the areas ruptured by the 1997 Umbria-  
379 Marche and the 2009 L'Aquila seismic sequences, with the patterns remaining relatively stationary  
380 during the AVN. Comparing the pre-sequence and sequence maps at 12 Hz shows the most significant  
381 temporal differences in patterns (**Figures 5, 6**). Before the sequence, the HS-HA are diffused and  
382 comprise the Visso and Norcia epicenters and the areas ruptured by the 1997 Umbria Marche  
383 (Colfiorito) and the 2009 L'Aquila sequences. Instead, there is a sharp separation between HS and  
384 HS-HA in the south and LS-HA in the north during the sequences. The boundary between zones is at  
385 a latitude of  $42.7^\circ$  N, corresponding to the lithological differences between the Umbria Marche and  
386 the Lazio-Abruzzi domains and part of the Monti Sibillini thrust.

## 387 **5. Discussions**

388 We discuss peak delay and  $Q_c^{-1}$  variations in space and time separately (**Figures 3,4**) and then use  
389 the parameter separation maps (**Figure 5**). These variations are investigated as a function of time and  
390 space for the pre-seismic and seismic periods. Spatial differences between the pre-seismic and the  
391 seismic phases characterize different processes, including fluid flow, crack opening/closure and crack  
392 density, pore pressure variations (compaction/dilatation), lithological contrasts and existing fault  
393 networks.

### 394 ***5.1 Peak Delay (scattering) patterns***

395 At all frequencies and for all sequences, a low-scattering NNE - SSW directed anomaly coincides  
396 with the Monti Sibillini thrust, including the Flysch of Laga Formation. Thus, the thrust appears as a  
397 low-scattering barrier for northern propagation of fluid-induced seismicity (Improta et al., 2019).  
398 High-scattering losses correspond to the carbonatic Gran Sasso massif and the L'Aquila basin  
399 (Chiaraluce et al., 2011), where the 2009 L'Aquila seismic sequence nucleated. These losses mark  
400 high velocity and density contrasts, high density of cracks and fractures, and basins in the upper part  
401 of the crust (Borleanu et al., 2017). The correspondence between high scattering and carbonate rocks  
402 fractured by historical sequences is analogue to that observed across the Lauria Mountains in  
403 Southern Italy (Napolitano et al., 2020).

404 Considering the relationship with the Gran Sasso and the Monti Sibillini thrust (**Figures 3a,b**), peak  
405 delays appear primarily sensitive to the existing structural elements (Calvet et al., 2013; De Siena et  
406 al., 2016) as the pre-existing thrust and active faults. This inference is supported by the spatial  
407 correlation with the velocity model of the Central Apennines of Chiarabba et al. (2020a). The authors  
408 show lateral heterogeneity across the Monti Sibillini thrust, with high  $V_P$  and  $V_P/V_S$  anomalies  
409 consistent with the high-scattering Lazio - Abruzzi domain and low  $V_P$  and  $V_P/V_S$  in the northern  
410 portion corresponding to the low-scattering Umbria - Marche domain.

411 Peak delays patterns change less than  $Q_c^{-1}$  patterns before and during the AVN at all frequencies  
412 (**Figures 3a,b** and **S10-12**). However, while high-scattering anomalies appear diffuse before the AVN  
413 at 1.5 Hz, they focus on a narrow NW-SE-striking band just south of the fault planes during the  
414 sequence (**Figure 3a**). Moving from the Amatrice to the Norcia sequences (**Figure 3b**), the high-  
415 scattering anomaly progressively expands from the southern fault plane to comprise the dense fault  
416 network located immediately to the SW of the modelled faults (red boxes in **Figure 3b**). We interpret  
417 this change in scattering attenuation as evidence of micro-fracturing processes within this network  
418 the fault network, lacking evidence of significant lithological change. This inference is supported by  
419 the higher-frequency peak delay maps (**Figures S11-12**).

## 420 **5.2 Coda $Q$ (absorption) patterns**

421 The sparse distribution of the high-absorption anomalies during the pre-sequence becomes a  
422 continuous NW-SE-striking pattern focused on the seismogenic zone during the AVN (**Figure 4a**).  
423 Spatial variations of high-absorption patterns are a manifestation of increased fluid content, with  
424 fluids expanding across the seismogenic zone with each sequence (**Figure 4b**). Fluids migrate across  
425 the faults at seismogenic depths (8-12 km), where the main events of the AVN occurred. Pastori et  
426 al. (2019) observed a reorientation of cracks from seismic anisotropy caused by overpressurized fluids  
427 trapped in the fault zones in the preparatory phase of the Norcia mainshock. The rock formations on  
428 the western side of the fault system are heavily fractured, and apparently, they channeled and trapped  
429 fluids. High-absorption anomalies focus primarily west of the activated fault system during the AVN  
430 (**Figure 4b**). They mark the extension of the highly fractured and fluid-filled zones and the area of  
431 maximum displacement recognized by Brozzetti et al. (2019) for the Monte Vettore fault.  
432 Our observations are consistent with the results from geochemical and geophysical studies that infer  
433 the critical role of CO<sub>2</sub>-rich deep fluids in the seismogenesis and evolution of seismic sequences  
434 across the Apennines (Miller et al., 2004; Di Luccio et al. 2010; Terakawa et al., 2010; Malagnini et  
435 al. 2012; Chiodini et al. 2004, 2020; Chiarabba et al., 2020b; Barberio et al., 2017). These studies

436 evidence a relation between CO<sub>2</sub> release and seismicity rates and locations (Miller et al., 2004;  
437 Chiodini et al., 2020). Such CO<sub>2</sub> is supposedly released from the mantle and accumulates at the  
438 boundary between the lower and upper crust. Here, overpressurized reservoirs develop, sealed by 10-  
439 12 km deep evaporitic levels (Chiodini et al., 2004, 2020; Chiarabba et al., 2020a). Indeed, an increase  
440 in the concentration of mineralized endogenic fluids corresponds to seismic sequences (Barberio et  
441 al., 2017). The source of these fluids has been identified in rocks located at a depth of about  
442 10 km (**Figure 1**). The influx of deep CO<sub>2</sub> could favor their formation and ascent to the surface.  
443 According to Di Luccio et al. (2010), these deep fluids mainly migrate along the NW-SE striking  
444 faults and fractures of the Central Apennines. This process is captured by the high-absorption patterns  
445 (**Figure 4b**).

446 This is the first time that geophysical responses to deep fluid migrations are identified along the  
447 seismogenic fractured zones of the Central Apennines. Our results do not exclude that those fluids  
448 could move in the shallower portion of the crust, especially where the permeability is higher, as within  
449 carbonates and basin filling deposits. Regardless, the maximum recorded water level variation in the  
450 Apennines aquifers during the AVN (e.g., Gran Sasso aquifer) is only 1.8 m (Devoti et al., 2018).

451 The absorption patterns evolve during the sequence as expected for high-absorption deep CO<sub>2</sub>-  
452 bearing fluids previously trapped in the fault systems (Miller et al., 2004). The development of a high-  
453 pressure front allows the propagation of fluids diffusing through the seismogenic zone and creating  
454 aftershocks. The absorption patterns show the evolution of this front from the location of the Amatrice  
455 earthquake towards the north and south when fluids diffuse across the fault planes (**Figure 4b**).  
456 Northern migration happened primarily during the Visso sequence, when the Monti Sibillini acted as  
457 a barrier (Improta et al., 2019). The Norcia sequence corresponds to the expansion of the  
458 overpressurized trapped fluids across the fractured region (Pastori et al., 2019), leading to the  
459 corresponding expanded absorption anomaly.

### 460 **5.3 Parameter map**

461 **Figure 5a,b** summarizes the combined spatial variation of scattering losses and absorption at 1.5 Hz.  
462 High-scattering and high-absorption patterns (red) correspond to the areas north of the 1997 Colfiorito  
463 earthquake and south of the 2009 L'Aquila earthquake before the sequence. This pattern is visible  
464 also at higher frequencies (12 Hz – **Figure 6a**). During the AVN, HS-HA concentrate on the southern  
465 and western portions of the seismogenic faults (red squares in **Figure 5a,b**). In the northern part of  
466 the epicentral area, high absorption (orange in **Figure 5a,b**) replaces the pre-sequence low scattering  
467 and low absorption patterns (green). This variation in time and space is consistent with the permeation  
468 of fluids across the northern portion of the seismogenic fault zones. However, the absence of  
469 scattering losses contrasts with the presence of wide fracture networks near the Visso epicenter and  
470 north of it. These networks are confined near, and specifically south and west of the other two  
471 mainshocks (**Figure 5b**, red). The structural models confirm that fluid pathways follow the direction  
472 of the maximum horizontal stress (Sibson, 2000), which in the Central Apennines is NW-SE-oriented  
473 and parallel to the strike of the active normal faults (Di Luccio et al., 2010). At higher frequencies  
474 (12 Hz), these pathways are not visible (**Figure 6**). High frequencies are more sensitive to small-scale  
475 features, and they cannot map variations of attenuation over wide tectonic structures. The  
476 consequence is that large-scale tectonic structures confine the inferred deep fluid flow and fracturing.  
477 **Figure 5b** details how fluids pervade the southern fault planes during the Amatrice sequence  
478 following the NW-SE preferred orientation of the faults and the elongation of Apennine belt. Yet,  
479 fracturing does not expand toward Visso, with the red patterns stopping around Norcia by the end of  
480 the AVN. The high-scattering and high-absorption pattern thus point to northern migrations of fluids  
481 along tectonic structures, associated with fracturing up to the Norcia epicenter.

## 482 **6. Conclusions**

483 The main results of this study are that:

- 484 1) Peak delay analysis delineates and characterizes the structural (e.g., Monti Sibillini thrust)  
485 and lithological (e.g., fractured carbonate rocks) domains of the Central Apennines over all

486 the studied frequency bands. High-scattering patterns highlight fracturing occurring during  
487 the AVN, with high-scattering anomalies focusing south and west of the seismogenic zone.

488 2) Coda-Q mapping marks the concentration of fluids across the seismogenic zone during the  
489 sequence. It detects a progression in time associated with fluid expansion from the Amatrice  
490 epicenter, mapping the migrations of deep CO<sub>2</sub>-rich fluids across the fractures and the fault  
491 networks of the Central Apennines.

492 3) Low-frequency parameter-space maps show the development of the fluid-filled fracture  
493 network, suggesting that large-scale tectonic structures constrain the deep fluids flow. Fluids  
494 permeate the northern fault region after the Visso earthquake. Still, wider fracturing was  
495 stopped by the Monti Sibillini structural boundary, so that fluids primarily expanded across  
496 the southern Norcia network in the last phase of the AVN.

497 These results point to a common feature for earthquake sequences occurring across the Central  
498 Apennines: the deep migration and expansion of CO<sub>2</sub>-bearing fluids along the NW-SE elongated  
499 seismogenic zone. The front and area of expansion of these processes are visible mapping attenuation  
500 mechanisms in time and space. Knowing their variations has a profound impact on assessing seismic  
501 hazard from earthquake ground motion in order to mitigate risk. Mapping scattering and absorption  
502 in the 3D space through seismic sequences could provide us with unprecedented sensitivity on  
503 structures and processes that lead to mainshocks and aftershocks in fault networks and their effect on  
504 earthquake ground motion amplitudes.

505

## 506 **Acknowledgments**

507 This work has been carried out in the framework of the project Pianeta Dinamico/2020-  
508 2021 supported by Ministero dell'Istruzione, dell'Università e della Ricerca (MIUR). Seismic  
509 waveforms were retrieved from the European Integrated Data Archive (EIDA) repository  
510 at <http://www.orfeus-eu.org/data/eida/> and from the Italian Accelerometric Archive  
511 at [http://itaca.mi.ingv.it/ItacaNet\\_30](http://itaca.mi.ingv.it/ItacaNet_30) (last accessed June 2016). The ITHACA catalogue used in this

512 paper can be found at: [http://www.isprambiente.gov.it/it/progetti/suolo-e-territorio-1/ithaca-](http://www.isprambiente.gov.it/it/progetti/suolo-e-territorio-1/ithaca-catalogo-delle-faglie-capaci)  
513 [catalogo-delle-faglie-capaci](http://www.isprambiente.gov.it/it/progetti/suolo-e-territorio-1/ithaca-catalogo-delle-faglie-capaci).

514 Murat2D is an open-access MATLAB<sup>®</sup> code available at <https://doi.org/10.5281/zenodo.5121429>.

515 Many of the plots were generated using the Generic Mapping Tools, version 4.2.1  
516 ([www.soest.hawaii.edu/gmt](http://www.soest.hawaii.edu/gmt), last accessed December 2008; Wessel and Smith, 1998) and using the  
517 Scientific Colour Maps (Cramer 2018; <http://doi.org/10.5281/zenodo.1243862>).

518

### 519 **CRedit authorship contribution statement**

520 **Simona Gabrielli**: Conceptualization, Methodology, Software, Writing- Original draft  
521 preparation, review, and editing. **Aybige Akinci**: Conceptualization, Data curation, Writing-  
522 Original draft preparation, review, and editing. **Guido Ventura**: Writing-Reviewing. **Ferdinando**  
523 **Napolitano**: Methodology, Writing. **Edoardo Del Pezzo**: Methodology, Validation. **Luca De**  
524 **Siena**: Conceptualization, Writing-Reviewing, Software.

525

### 526 **References**

527 Aki, K., Chouet, B. (1975). Origin of coda waves: Source, attenuation, and scattering effects. *J.*  
528 *Geophys. Res.* 80, 3322–3342. <https://doi.org/10.1029/JB080i023p03322>

529 Akinci, A., Pezzo, E.D., Malagnini, L. (2020). Intrinsic and scattering seismic wave attenuation  
530 in the Central Apennines (Italy). *Phys. Earth Planet. Inter.* 303.  
531 <https://doi.org/10.1016/j.pepi.2020.106498>

532 Amoruso, A., Crescentini, L., Petitta, M., Rusi, S., Tallini, M. (2011). Impact of the 6 April 2009  
533 L'Aquila earthquake on groundwater flow in the Gran Sasso carbonate aquifer, Central  
534 *Italy Hydrological Processes*, 25(11), 1754-1764. <https://doi.org/10.1002/hyp.7933>

535 Barberio, M. D., Barbieri, M., Billi, A., Doglioni, C., & Petitta, M. (2017). Hydrogeochemical  
536 changes before and during the 2016 Amatrice-Norcia seismic sequence (central Italy).  
537 *Scientific reports*, 7(1), 1-12. <https://doi.org/10.1038/s41598-017-11990-8>

538 Billi, A., Tiberti, M.M. (2009). Possible causes of arc development in the Apennines, central  
539 Italy. *Bull. Geol. Soc. Am.* 121, 1409–1420. <https://doi.org/10.1130/B26335.1>

- 540 Borleanu, F., De Siena, L., Thomas, C., Popa, M., Radulian, M. (2017). Seismic scattering and  
 541 absorption mapping from intermediate-depth earthquakes reveals complex tectonic  
 542 interactions acting in the Vrancea region and surroundings (Romania). *Tectonophysics* 706,  
 543 129–142.
- 544 Brozzetti, F., Cirillo, D., de Nardis, R., Cardinali, M., Lavecchia, G., Orecchio, B., Totaro, C.  
 545 (2017). Newly identified active faults in the Pollino seismic gap, southern Italy, and their  
 546 seismotectonic significance. *Journal of Structural Geology*, 94, 13-31.
- 547 Brozzetti, F., Boncio, P., Cirillo, D., Ferrarini, F., De Nardis, R., Testa, A., Lavecchia, G. (2019).  
 548 High-resolution field mapping and analysis of the August–October 2016 coseismic surface  
 549 faulting (central Italy earthquakes): Slip distribution, parameterization, and comparison  
 550 with global earthquakes. *Tectonics*, 38(2), 417-439.
- 551 Buttinelli, M., Pezzo, G., Valoroso, L., De Gori, P., Chiarabba, C. (2018). Tectonics Inversions,  
 552 Fault Segmentation, and Triggering Mechanisms in the Central Apennines Normal Fault  
 553 System: Insights from High-Resolution Velocity Models. *Tectonics* 37, 4135–4149.  
 554 <https://doi.org/10.1029/2018TC005053>
- 555 Calvet, M., Margerin, L. (2013). Lapse-time dependence of coda Q: Anisotropic multiple-  
 556 scattering models and application to the Pyrenees. *Bull. Seismol. Soc. Am.* 103, 1993–2010.  
 557 <https://doi.org/10.1785/0120120239>
- 558 Calvet, M., Sylvander, M., Margerin, L., Villaseñor, A. (2013). Spatial variations of seismic  
 559 attenuation and heterogeneity in the Pyrenees: Coda Q and peak delay time analysis.  
 560 *Tectonophysics* 608, 428–439. <https://doi.org/10.1016/j.tecto.2013.08.045>
- 561 Carminati E., Doglioni C. (2012). Alps vs. Apennines: the paradigm of a tectonically asymmetric  
 562 Earth. *Earth Sci Rev* 112:67–96.
- 563 Carminati, E., Bignami, C., Doglioni, C., Smeraglia, L. (2020). Lithological control on multiple  
 564 surface ruptures during the 2016–2017 Amatrice-Norcia seismic sequence. *J. Geodyn.* 134.  
 565 <https://doi.org/10.1016/j.jog.2019.101676>
- 566 Chiarabba, C., Piccinini, D. and De Gori, P. (2009a). Velocity and attenuation tomography of  
 567 the Umbria Marche 1997 fault system: evidence of a fluid-governed seismic sequence.  
 568 *Tectonophysics*, 476(1-2), pp.73-84. <https://doi.org/10.1016/j.tecto.2009.04.004>
- 569 Chiarabba, C., Amato, A., Anselmi, M., Baccheschi, P., Bianchi, I., Cattaneo, M., Cecere, G.,  
 570 Chiaraluce, L., Ciaccio, M.G., De Gori, P., De Luca, G., Di Bona, M., Di Stefano, R.,  
 571 Faenza, L., Govoni, A., Improta, L., Lucente, F.P., Marchetti, A., Margheriti, L., Mele, F.,  
 572 Michelini, A., Monachesi, G., Moretti, M., Pastori, M., Piana Agostinetti, N., Piccinini, D.,  
 573 Roselli, P., Seccia, D., Valoroso, L. (2009b). The 2009 L’Aquila (central Italy) Mw6.3

- 574 earthquake: main shock and aftershocks. *Geophys. Res. Lett.* 36.  
 575 <https://doi.org/10.1029/2009GL039627>
- 576 Chiarabba, C., Buttinelli, M., Cattaneo, M., De Gori, P. (2020a). Large Earthquakes Driven by  
 577 Fluid Overpressure: The Apennines Normal Faulting System Case. *Tectonics* 39.  
 578 <https://doi.org/10.1029/2019TC006014>
- 579 Chiarabba, C., De Gori, P., Segou, M., & Cattaneo, M., (2020b). Seismic velocity precursors to  
 580 the 2016 Mw 6.5 Norcia (Italy) earthquake. *Geology*, 48(9), 924-928.
- 581 Chiaraluce, L., Amato, A., Cocco, M., Chiarabba, C., Selvaggi, G., Di Bona, M., Piccinini, D.,  
 582 Deschamps, A., Margheriti, L., Courboux, F., Ripepe, M. (2004). Complex Normal  
 583 Faulting in the Apennines Thrust-and-Fold Belt: The 1997 Seismic Sequence in Central  
 584 Italy, *Bulletin of the Seismological Society of America*.
- 585 Chiaraluce, L., Chiarabba, C., Collettini, C., Piccinini, D. and Cocco, M. (2007). Architecture  
 586 and mechanics of an active low-angle normal fault: Alto Tiberina fault, northern  
 587 Apennines, Italy. *Journal of Geophysical Research: Solid Earth*, 112(B10).  
 588 <https://doi.org/10.1029/2007JB005015>
- 589 Chiaraluce, L., Chiarabba, C., De Gori, P., Di Stefano, R., Improta, L., Piccinini, D.,  
 590 Schlagenhauf, A., Traversa, P., Valoroso, L., Voisin, C. (2011). The 2009 L'Aquila (central  
 591 Italy) seismic sequence. *Boll. di Geofis. Teor. ed Appl.* 52, 367–387.  
 592 <https://doi.org/10.4430/bgta0019>
- 593 Chiaraluce, L., Di Stefano, R., Tinti, E., Scognamiglio, L., Michele, M., Casarotti, E., Cattaneo,  
 594 M., De Gori, P., Chiarabba, C., Monachesi, G., Lombardi, A., Valoroso, L., Latorre, D.,  
 595 Marzorati, S. (2017). The 2016 central Italy seismic sequence: A first look at the  
 596 mainshocks, aftershocks, and source models. *Seismol. Res. Lett.*  
 597 <https://doi.org/10.1785/0220160221>
- 598 Chiodini, G., Cardellini, C., Amato, A., Boschi, E., Caliro, S., Frondini, F. and Ventura, G.  
 599 (2004). Carbon dioxide Earth degassing and seismogenesis in central and southern Italy.  
 600 *Geophysical Research Letters*, 31(7). <https://doi.org/10.1029/2004GL019480>
- 601 Chiodini, G., Caliro, S., Cardellini, C., Frondini, F., Inguaggiato, S. and Matteucci, F. (2011).  
 602 Geochemical evidence for and characterization of CO<sub>2</sub> rich gas sources in the epicentral  
 603 area of the Abruzzo 2009 earthquakes. *Earth and Planetary Science Letters*, 304(3-4),  
 604 pp.389-398. <https://doi.org/10.1016/j.epsl.2011.02.016>
- 605 Chiodini, G., Cardellini, C., Di Luccio, F., Selva, J., Frondini, F., Caliro, S., ... & Ventura, G.  
 606 (2020). Correlation between tectonic CO<sub>2</sub> Earth degassing and seismicity is revealed by a  
 607 10-year record in the Apennines, Italy. *Science advances*, 6(35), eabc2938.

- 608 Collettini, C., Cardellini, C., Chiodini, G., De Paola, N., Holdsworth, R.E. and Smith, S.A.F.  
 609 (2008). Fault weakening due to CO<sub>2</sub> degassing in the Northern Apennines: Short-and long-  
 610 term processes. *Geological Society*, London, Special Publications, 299(1), pp.175-194.  
 611 <https://doi.org/10.1144/SP299.11>
- 612 de Lorenzo, S., Del Pezzo, E. and Bianco, F. (2013). QC, Q $\beta$ , Qi and QS attenuation parameters  
 613 in the Umbria–Marche (Italy) region. *Physics of the Earth and Planetary Interiors*, 218,  
 614 pp.19-30. <https://doi.org/10.1016/j.pepi.2013.03.002>
- 615 De Siena, L., Amoroso, A., Pezzo, E. Del, Wakeford, Z., Castellano, M., Crescentini, L. (2017).  
 616 Space-weighted seismic attenuation mapping of the aseismic source of Campi Flegrei  
 617 1983-1984 unrest. *Geophys. Res. Lett.* 44, 1740–1748.  
 618 <https://doi.org/10.1002/2017GL072507>
- 619 De Siena, L., Calvet, M., Watson, K.J., Jonkers, A.R.T., Thomas, C. (2016). Seismic scattering  
 620 and absorption mapping of debris flows, feeding paths, and tectonic units at Mount St.  
 621 Helens volcano. *Earth Planet. Sci. Lett.* 442, 21–31.  
 622 <https://doi.org/10.1016/j.epsl.2016.02.026>
- 623 Del Pezzo, E., De La Torre, A., Bianco, F., Ibanez, J., Gabrielli, S., De Siena, L. (2018).  
 624 Numerically calculated 3d space-weighting functions to image crustal volcanic structures  
 625 using diffuse coda waves. *Geosci.* 8. <https://doi.org/10.3390/geosciences8050175>
- 626 Devoti, R., Riguzzi, F., Cinti, F.R., Ventura, G. (2018). Long-term strain oscillations related to  
 627 the hydrological interaction between aquifers in intra-mountain basins: A case study from  
 628 Apennines chain (Italy). *Earth Planet. Sci. Lett.* 501, 1–12.  
 629 <https://doi.org/10.1016/j.epsl.2018.08.014>
- 630 Di Bucci, D., Buttinelli, M., D’Ambrogio, C., Scrocca, D., Anzidei, M., Basili, R., Bigi, S.,  
 631 Bignami, C., Bonini, L., Bonomo, R. and Burrato, P. (2021). RETRACE-3D project: a  
 632 multidisciplinary collaboration to build a crustal model for the 2016-2018 central Italy  
 633 seismic sequence. *Bollettino di Geofisica Teorica e Applicata*.  
 634 <https://doi.org/10.4430/bgta0343>
- 635 Di Luccio, F., Ventura, G., Di Giovambattista, R., Piscini, A., Cinti, F.R. (2010). Normal faults  
 636 and thrusts reactivated by deep fluids: The 6 April 2009 Mw 6.3 L’Aquila earthquake,  
 637 central Italy. *J. Geophys. Res. Solid Earth* 115. <https://doi.org/10.1029/2009JB007190>
- 638 Doglioni, C., Barba, S., Carminati, E., Riguzzi, F. (2014). Fault on-off versus coseismic fluids  
 639 reaction. *Geosci. Front.* 5, 767–780. <https://doi.org/10.1016/j.gsf.2013.08.004>

- 640 Gabrielli, S., De Siena, L., Napolitano, F., & Del Pezzo, E. (2020). Understanding seismic path  
641 biases and magmatic activity at Mount St Helens volcano before its 2004  
642 eruption. *Geophysical Journal International*, 222(1), 169-188.
- 643 Improta, L., Latorre, D., Margheriti, L., Nardi, A., Marchetti, A., Lombardi, A.M., Castello, B.,  
644 Villani, F., Ciaccio, M.G., Mele, F.M., Moretti, M., Battelli, P., Berardi, M., Castellano,  
645 C., Melorio, C., Modica, G., Pirro, M., Rossi, A., Thermes, C., Pagliuca, N., Spadoni, S.,  
646 Arcoraci, L., Battelli, A., Lisi, A., Pizzino, L., Baccheschi, P., Cantucci, B., Sciarra, A.,  
647 Bono, A., Marcocci, C., Lauciani, V., Mandiello, A., Pintore, S., Quintiliani, M., Frepoli,  
648 A., Colini, L., Pinzi, S., Scognamiglio, L., Basili, A., D'Addezio, G., Sgroi, T., Smedile,  
649 A., Montuori, C., Tardini, R., Tozzi, R., Monna, S., Miconi, L., Mariucci, M.T., Di Maro,  
650 R. (2019). Multi-segment rupture of the 2016 Amatrice-Visso-Norcia seismic sequence  
651 (central Italy) constrained by the first high-quality catalog of Early Aftershocks. *Sci. Rep.*  
652 9. <https://doi.org/10.1038/s41598-019-43393-2>
- 653 Malagnini, L., Lucente, F.P., De Gori, P., Akinci, A., Munafo', I. (2012). Control of pore fluid  
654 pressure diffusion on fault failure mode: Insights from the 2009 L'Aquila seismic sequence.  
655 *J. Geophys. Res. Solid Earth* 117. <https://doi.org/10.1029/2011JB008911>
- 656 Mayor, J., Calvet, M., Margerin, L., Vanderhaeghe, O., & Traversa, P. (2016). Crustal structure  
657 of the Alps as seen by attenuation tomography. *Earth and Planetary Science Letters*, 439,  
658 71-80. <https://doi.org/10.1016/j.epsl.2016.01.025>
- 659 Miller, S. A., Collettini, C., Chiaraluce, L., Cocco, M., Barchi, M., & Kaus, B. J. (2004).  
660 Aftershocks driven by a high-pressure CO<sub>2</sub> source at depth. *Nature*, 427(6976), 724-727.
- 661 Montone, P., & Mariucci, M. T. (2016). The new release of the Italian contemporary stress  
662 map. *Geophysical Journal International*, 205(3), 1525-1531.
- 663 Napolitano, F., De Siena, L., Gervasi, A., Guerra, I., Scarpa, R., La Rocca, M. (2020). Scattering  
664 and absorption imaging of a highly fractured fluid-filled seismogenetic volume in a region  
665 of slow deformation. *Geosci. Front.* 11, 989–998.  
666 <https://doi.org/10.1016/j.gsf.2019.09.014>
- 667 Paasschens, J. (1997). Solution of the time-dependent Boltzmann equation. *Phys. Rev. E* 56,  
668 1135–1141. <https://doi.org/10.1103/PhysRevE.56.1135>
- 669 Pacheco, C., Snieder, R. (2005). Time-lapse travel time change of multiply scattered acoustic  
670 waves. *J. Acoust. Soc. Am.* 118, 1300–1310. <https://doi.org/10.1121/1.2000827>
- 671 Pastori, M., Baccheschi, P., Margheriti, L. (2019). Shear Wave Splitting Evidence and Relations  
672 with Stress Field and Major Faults From the “Amatrice-Visso-Norcia Seismic Sequence.”  
673 *Tectonics* 38, 3351–3372. <https://doi.org/10.1029/2018TC005478>

- 674 Saito, T., Sato, H., & Ohtake, M. (2002). Envelope broadening of spherically outgoing waves in  
675 three-dimensional random media having power law spectra. *Journal of Geophysical*  
676 *Research: Solid Earth*, 107(B5), ESE-3.
- 677 Sato, H., Fehler, M.C., Maeda, T. (2012). Seismic Wave Propagation and Scattering in the  
678 Heterogeneous Earth: Second Edition. *Springer*, New York, USA.
- 679 Shapiro, N.M., Campillo, M., Margerin, L., Singh, S.K., Kostoglodov, V. and Pacheco, J.  
680 (2000). The energy partitioning and the diffusive character of the seismic coda. *Bulletin of*  
681 *the Seismological Society of America*, 90(3), pp.655-665.  
682 <https://doi.org/10.1785/0119990021>
- 683 Sketsiou, P., Napolitano, F., Zenonos, A., De Siena, L. (2020). New insights into seismic  
684 absorption imaging. *Phys. Earth Planet. Inter.* 298.  
685 <https://doi.org/10.1016/j.pepi.2019.106337>
- 686 Takahashi, T., Sato, H., Nishimura, T., & Obara, K. (2007). Strong inhomogeneity beneath  
687 Quaternary volcanoes revealed from the peak delay analysis of S-wave seismograms of  
688 microearthquakes in northeastern Japan. *Geophysical Journal International*, 168(1), 90-99.
- 689 Ventura, G., Di Giovambattista, R. (2013). Fluid pressure, stress field and propagation style of  
690 coalescing thrusts from the analysis of the 20 May 2012 ML 5.9 Emilia earthquake  
691 (Northern Apennines, Italy). *Terra Nov.* 25, 72–78. <https://doi.org/10.1111/ter.12007>
- 692 Walters, R.J., Gregory, L.C., Wedmore, L.N.J., Craig, T.J., McCaffrey, K., Wilkinson, M.,  
693 Chen, J., Li, Z., Elliott, J.R., Goodall, H., Iezzi, F., Livio, F., Michetti, A.M., Roberts, G.,  
694 Vittori, E. (2018). Dual control of fault intersections on stop-start rupture in the 2016  
695 Central Italy seismic sequence. *Earth Planet. Sci. Lett.* 500, 1–14.  
696 <https://doi.org/10.1016/j.epsl.2018.07.043>.

697

698

699

700

701

702 **Table 1.**  $Q_c^{-1}$  for the two main dataset, with their associated standard deviation  $\sigma$ , obtained from  
 703 the linear regression (**Figure S4**) at each frequency band. \* and # are the dependence of  $Q_c^{-1}$  vs.  
 704 frequency for the Pre-Sequence and 2016-2017 Sequence, respectively.

705

$f$ (Hz)	Pre-Sequence (* ) $Q_c^{-1} \pm \sigma$	2016-2017 Sequence (# ) $Q_c^{-1} \pm \sigma$
1.5	$0.006 \pm 0.003$	$0.006 \pm 0.003$
3	$0.003 \pm 0.001$	$0.003 \pm 0.001$
6	$0.0020 \pm 0.0006$	$0.0020 \pm 0.0005$
12	$0.0011 \pm 0.0005$	$0.0011 \pm 0.0004$

706 (\* )  $Q_c^{-1} = (0.0075 \pm 0.0007) f^{(-0.74 \pm 0.10)}$ ; (#)  $Q_c^{-1} = (0.0076 \pm 0.0005) f^{(-0.76 \pm 0.07)}$

707

708

709

710

711

712

713

714

715

716

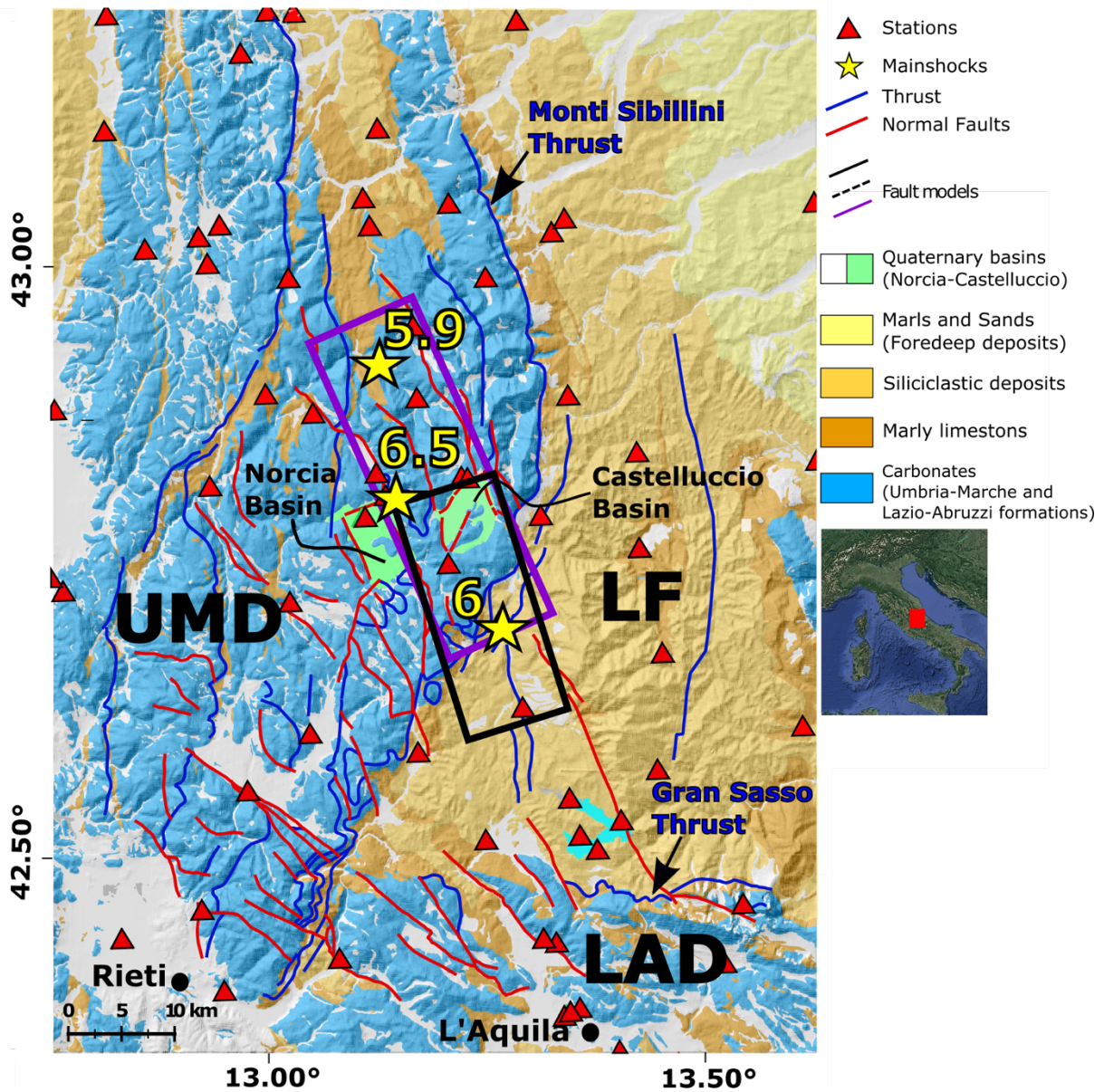
717

718

719

720

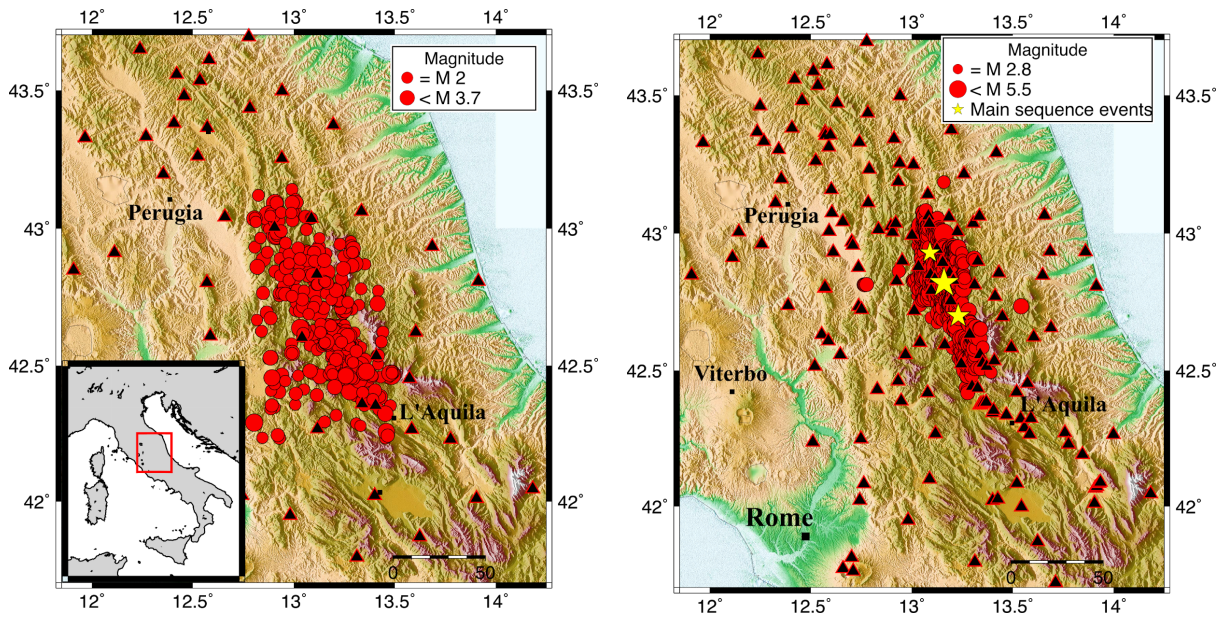
721

722 **Figures**

723

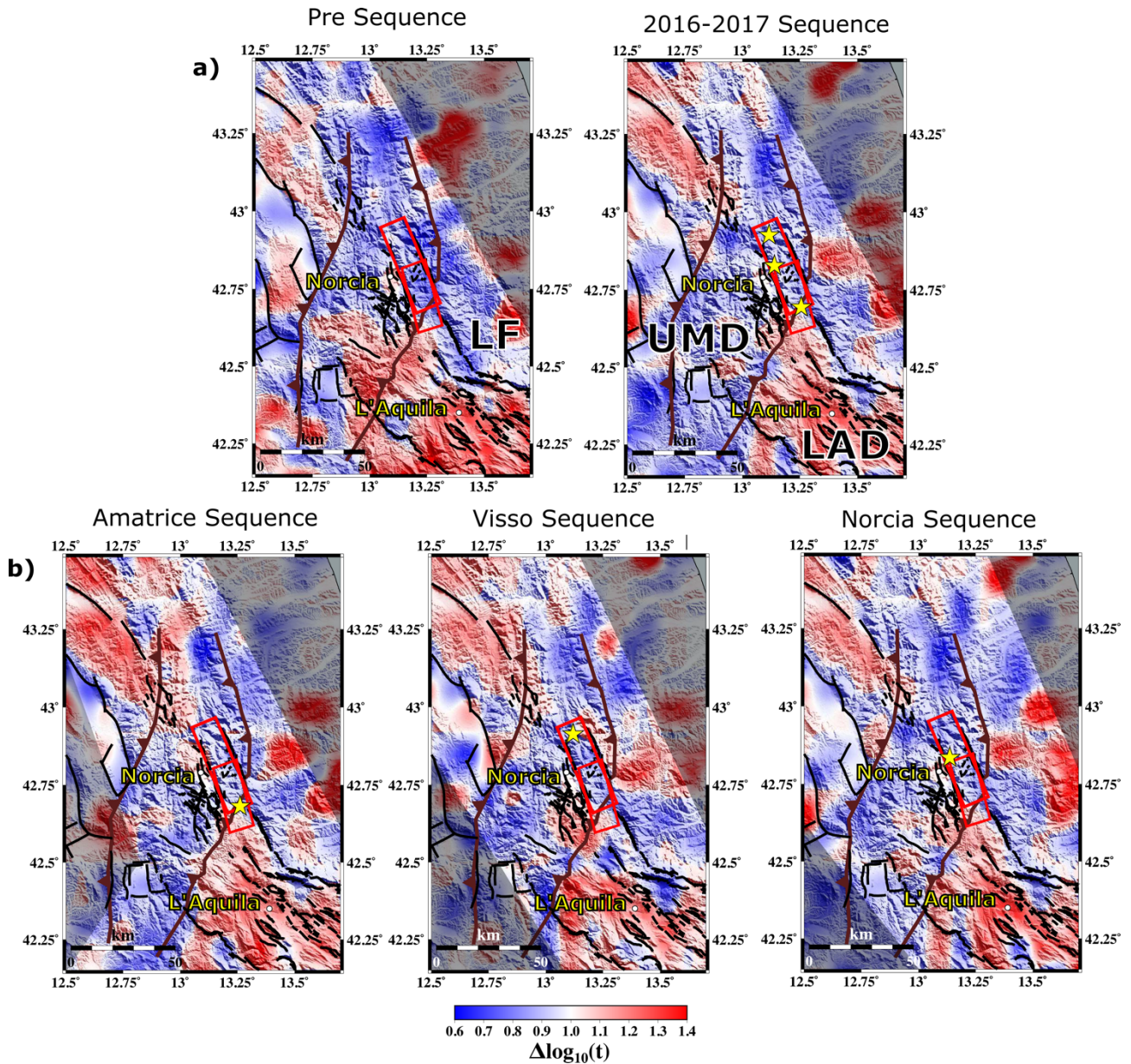
724 *Figure 1 Simplified geological map of Central Italy (after Di Bucci et al. 2021). In blue, the*  
 725 *carbonates of the Umbria-Marche (UMD) and Lazio-Abruzzi (LAD) domains; in yellow, the foredeep*  
 726 *domain (LF - Laga formation). The seismic network used for the sequence period is represented with*  
 727 *red triangles. Yellow stars correspond to the Amatrice ( $M_w6$ ), Visso ( $M_w5.9$ ) and Norcia ( $M_w6.5$ )*  
 728 *mainshocks. The black and purple boxes are the Amatrice and Norcia fault planes respectively. Study*  
 729 *area within the Italian Peninsula framework is shown in the inset on the right panel.*

730



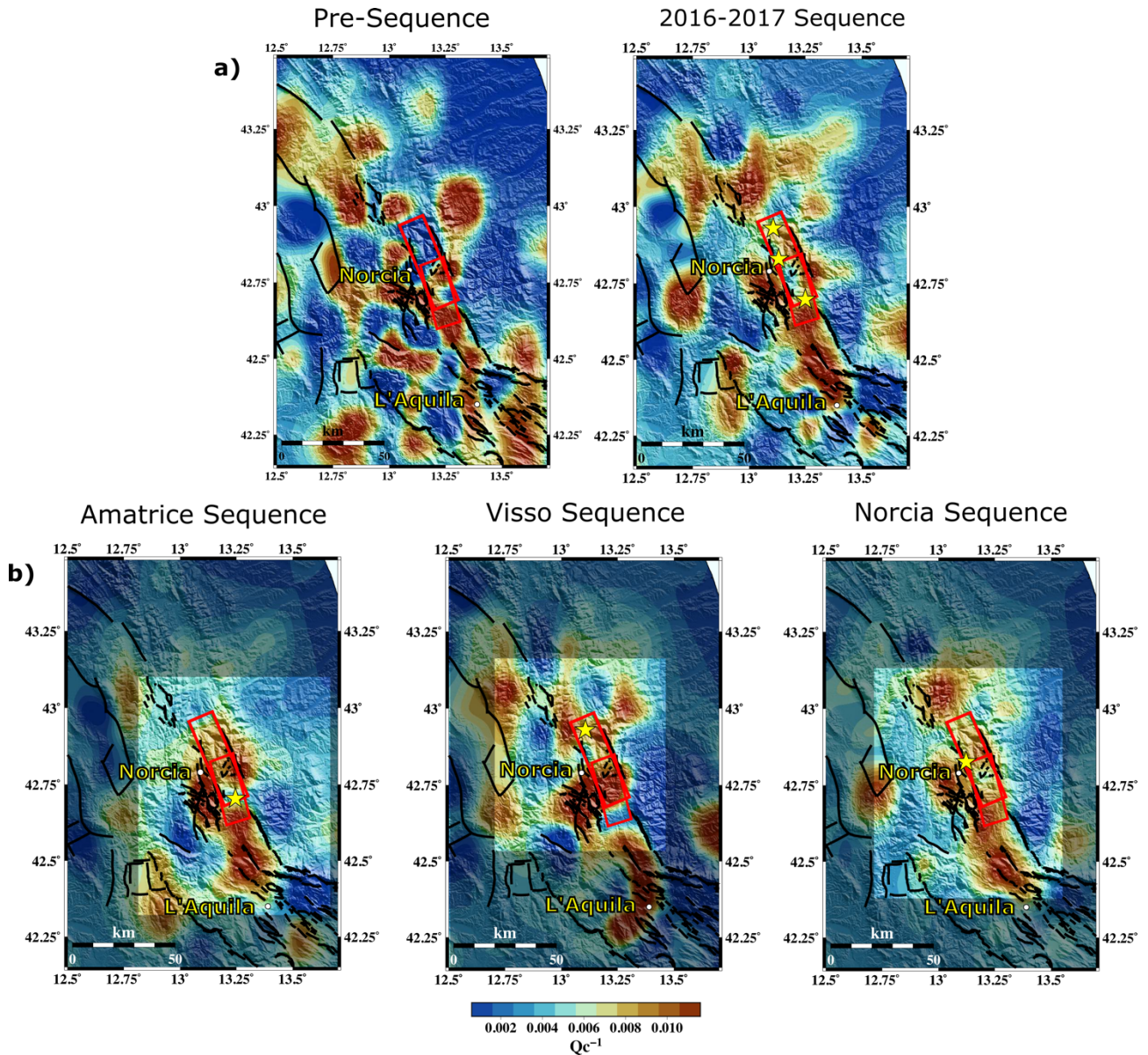
731

732 *Figure 2 Dataset used for the analysis and the seismic network for the pre-sequence (left), and the*  
 733 *Amatrice - Visso - Norcia sequence (right). Black triangles represent the stations; red circles the*  
 734 *seismic events; stars indicate the main events (Amatrice - Visso - Norcia) of the 2016 - 2017 seismic*  
 735 *sequence. Study area in the lower-left panel in the Italian Peninsula framework.*



736

737 *Figure 3 Spatial and temporal variation of Peak Delay at  $f_c = 1.5$  Hz over the a) Pre-sequence, the*  
 738 *2016-2017 sequence and b) three individual sequences time frames. Red boxes are the fault plane for*  
 739 *the Amatrice and the Norcia earthquakes and black lines the faults from ITHACA catalogue. Brown*  
 740 *lines are the main thrust of the area. The stars indicate the main shocks of each 2016-2017 sequence.*  
 741 *The maps have been restricted to the area of interest. The main geological domains are highlighted:*  
 742 *LF - Laga Formation; UMD - Umbria-Marche Domain; LAD - Lazio-Abruzzi Domain.*



743

744 *Figure 4 Spatial variation of  $Q_c^{-1}$  at  $f_c = 1.5$  Hz for the a) Pre-sequence and the 2016-2017 sequence*

745 *and b) three individual sequences time frames. Red boxes are the fault plane activated during the*

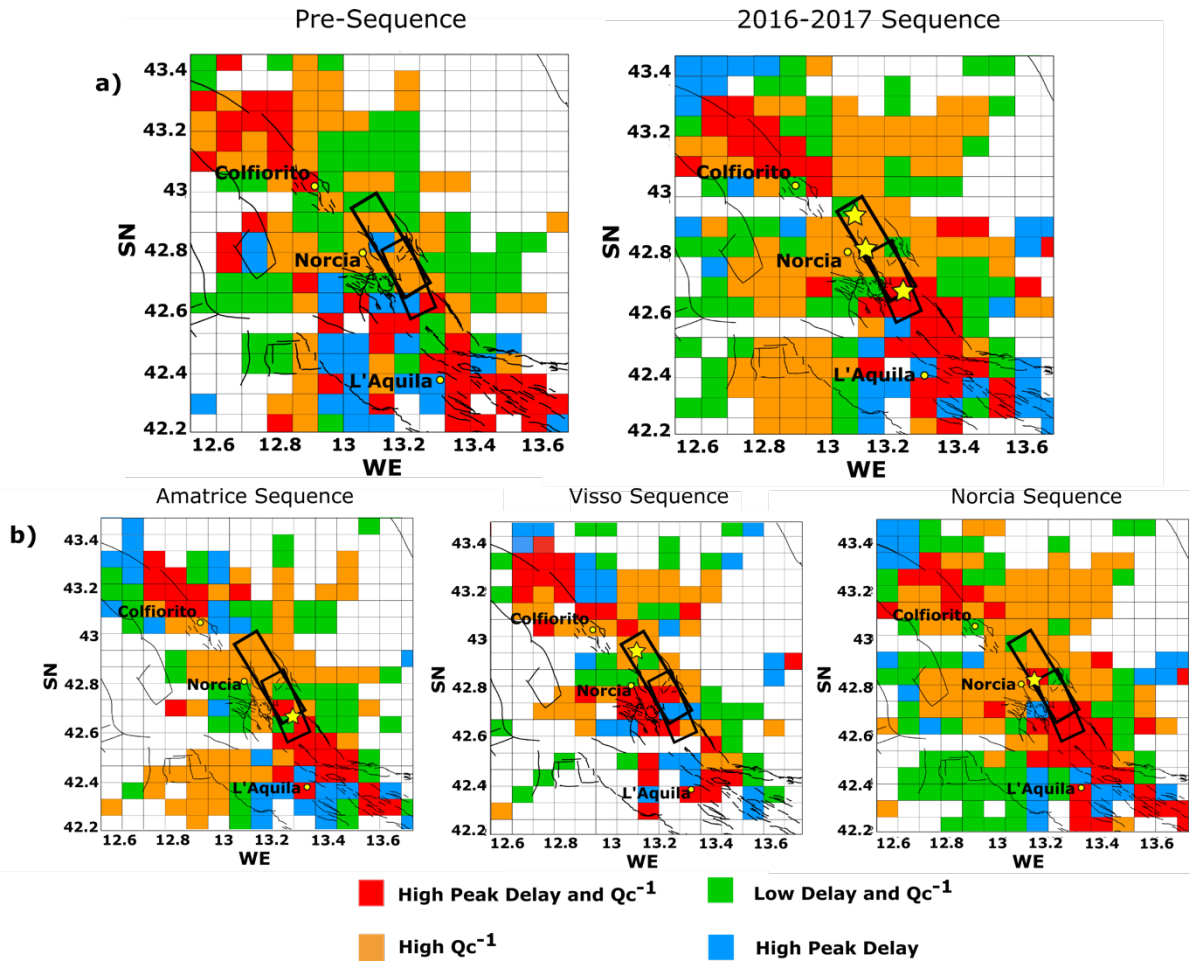
746 *AVN sequence and the black lines are the fault lines from the ITHACA catalogue. The stars indicate*

747 *the main shocks of each 2016-2017 sequence. The maps have been restricted to the area of interest*

748 *and the gray masks are covering the areas unresolved by the checkerboard tests at each sequence.*

749

750



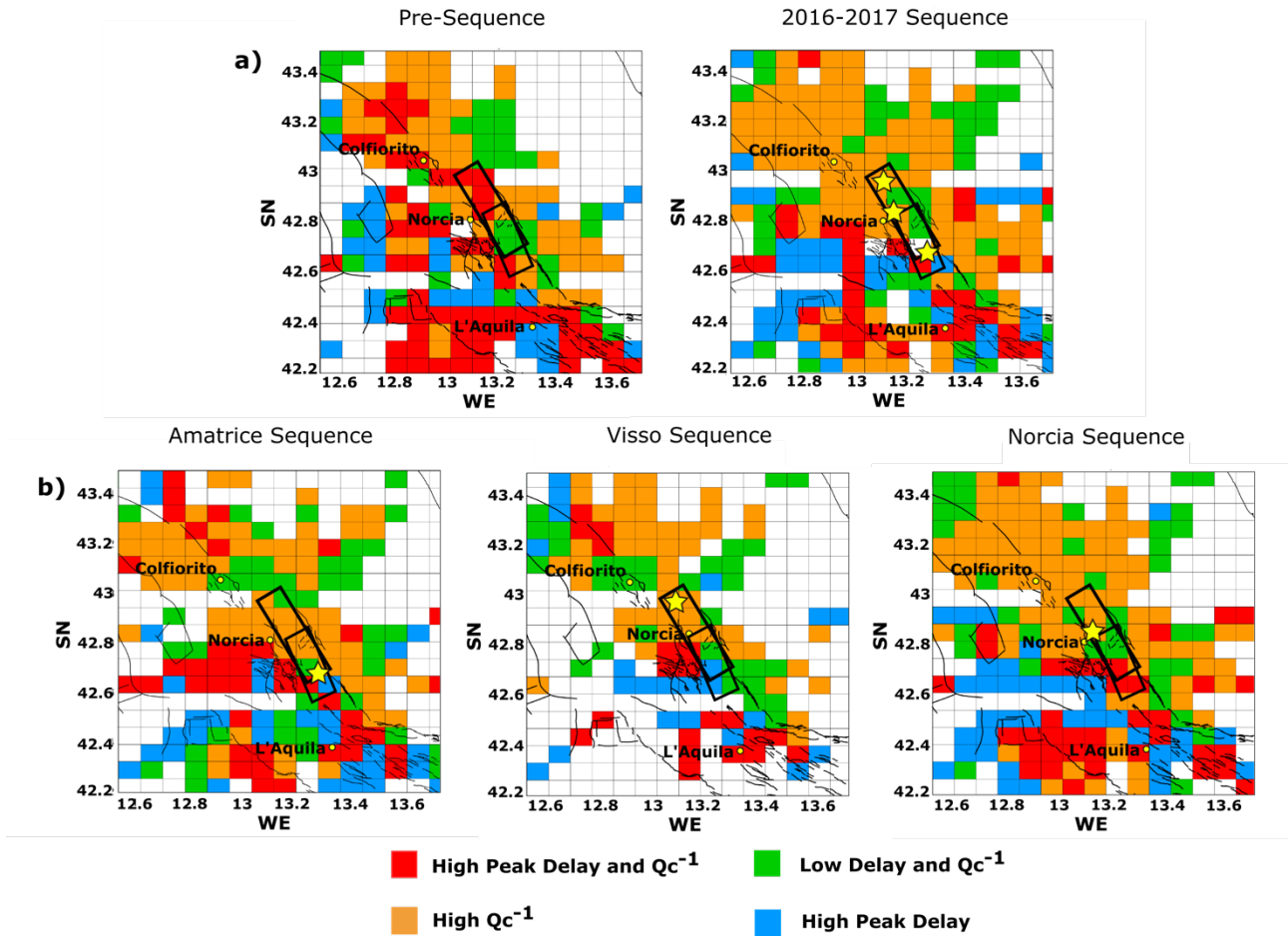
751  
752

753

754 *Figure 5 Parameter separation map at  $f_c = 1.5$  Hz of the a) Pre-sequence and the 2016-2017 sequence*  
 755 *and b) three individual sequences time frames. The red color for high scattering and high absorption*  
 756 *(HS-HA), orange for low scattering and increased absorption (LS-HA), light blue for high scattering*  
 757 *and low absorption (HS-LA), green for low scattering and low absorption (LS-LA), and white for the*  
 758 *areas with a level of discrimination less than 1% of the maximum variations.*

759

760



761

762

763 *Figure 6 Parameter separation map at  $f_c = 12$  Hz of the a) Pre-sequence and the 2016-2017 sequence*  
 764 *and b) three individual sequences time frames. The red color for high scattering and high absorption*  
 765 *(HS-HA), orange for low scattering and increased absorption (LS-HA), light blue for high scattering*  
 766 *and low absorption (HS-LA), green for low scattering and low absorption (LS-LA), and white for the*  
 767 *areas with a level of discrimination less than 1% of the maximum variations.*